IEEE Access
Multidisciplinary | Rapid Review | Open Access Journal

Received January 9, 2020, accepted January 26, 2020, date of publication February 10, 2020, date of current version February 20, 2020.

Digital Object Identifier 10.1109/ACCESS.2020.2973046

NLOS Target Localization Behind an L-Shaped Corner With an L-Band UWB Radar

XIAQING YANG[1], (Student Member, IEEE), SHIHAO FAN[1], SHISHENG GUO[1], (Member, IEEE), SONGLIN LI[1], GUOLONG CUI[1], (Senior Member, IEEE), AND WEI ZHANG[1,2]

[1]School of Information and Communication Engineering, University of Electronic Science and Technology of China, Chengdu 611731, China
[2]Science and Technology on Electronic Information Control Laboratory, Chengdu 610036, China

Corresponding author: Shisheng Guo (shishengG@std.uestc.edu.cn)

This work was supported in part by the National Natural Science Foundation of China under Grant 61871080, Grant 61771109, and Grant 61701093, in part by the Changjiang Scholar Program, in part by the 111 Project under Grant B17008, in part by the Science and Technology Department of Sichuan Province Miaozi Project under Grant 2019JDRC0061, and in part by the GF Science and Technology Special Innovation Zone Project.

ABSTRACT For the reason of target multipaths ambiguities, localization for hidden moving target due to lack of line of sight (LOS) path in urban environments is a hard task. To handle this problem we propose a localization algorithm based on the internal connection of these multipaths in this paper. First, we establish an electromagnetic (EM) propagation model based on the characters of the measured signal received by an L-band single-input single-output (SISO) ultra-wideband (UWB) radar. After that, the model-based target localization algorithm is proposed based on a times-of-arrival (TOAs) association method, which is able to match the measured TOAs with the corresponding EM propagation paths correctly. The proposed method can cope with the case while some missing detections of TOAs happen. Simulation and experimental results ultimately validate the robustness and the state-of-the-art performance of the proposed algorithm.

INDEX TERMS NLOS target localization, corner environment, UWB radar, multipath exploitation.

I. INTRODUCTION

Urban sensing has wide applications in many fields, such as urban battles, rescues and anti-terrorism [1]–[3]. The EM waves in these scenarios often fail to reach the hidden target along the line of sight (LOS) path for the reason of the obstructions surrounded. The traditional LOS detection methods are thus no longer effective under this circumstance. Intuitively, non-LOS (NLOS) hidden target detection was then proposed and has attracted considerable attention [4]–[24].

Among the NLOS detections, through-the-wall detection which exploits the penetrating signal to detect the target has been studied for many years [4]–[9]. However, the penetrating signals are very weak while the target is hidden behind the whole room or at the building corner due to the serious attenuation while passing multiple walls. Under this situation, the NLOS multipath detection is more qualified for NLOS detection by exploiting the multipaths derived from diffraction and specular reflections on building surfaces.

The associate editor coordinating the review of this manuscript and approving it for publication was Hasan S. Mir.

There have been many works done in exploiting NLOS multipaths to detect hidden targets [10]–[24]. In [10]–[13], the multipath returns received by the X-band radar were utilized to obtain the micro-Doppler features from moving targets. In [14], Zetik *et al.* proposed a one-dimensional target localization method based on a UWB sensor operated in the frequency band from C-band to X-band. As a continuation of this work, the two-dimensional target location was obtained using the multipaths derived from the diffraction path and a combination of the once-reflection path and the diffraction path [15]. In addition, several articles have exploited the millimeter wave radar to detect the hidden targets [16]–[18]. In [17], a detection and localization algorithm based on the matched subspace filter method was developed, and in [18], Zhao *et al.* proposed a phase comparison based target localization algorithm by exploiting the phase differences of the multipaths among multiple channels of a single-input multiple-output (SIMO) millimeter wave radar. Furthermore, the feasibility of NLOS targets detection by terahertz waves have been demonstrated in [19]. Some works have been carried out to detect the concealed target based on laser radars [20]–[24]. Specifically, an ultrafast transient

imaging method was proposed in [20] and Manna *et al.* developed two iterative back-projection algorithms to acquire the NLOS target image in [21]. In [23], a new NLOS imaging system was presented to collect the time-of-flight information of the target and then reconstructed the image of the target. This system provided significant improvements in terms of power requirements, form factor, cost, and reconstruction time, while still maintaining a comparable time resolution.

In summary, the NLOS multipath detection can be achieved by using various bands of EM waves. However, the EM waves of the above bands can't penetrate the wall for target detection, which limits the function of the radar in complex environments. In this paper, we consider a dual-use band (L-band) to detect the NLOS target. Different from the cases in [9]–[23], for L-band radar, there are different EM propagation characteristics. In our previous work [25], we have obtained the wall's positions in corner environment using an L-band imaging radar, while in [26], a positioning algorithm which utilize multipath components produced by diffraction and specular reflections on surrounding surfaces is proposed. It is worth mentioning that this paper is an extension of our work in [26]. We first analyze the characters of the measured signal of an L-shape corner scenario which is received by an L-band UWB radar and establish an EM propagation model. Then, a model-based target localization algorithm is proposed, based on a TOAs association method which can match the measured TOAs with the corresponding propagation paths correctly. The proposed method is able to achieve good NLOS target localization performance even while some missed detections of TOAs appear.

The rest of the paper is organized as follows. In Section II, the EM wave propagation model in an L-shaped corner scenario is established. The target localization algorithm based on a TOAs association method is proposed in Section III. In Section IV, numerical simulations and experiments data validate the proposed algorithm and Section V ultimately concludes this paper.

II. EM WAVE PROPAGATION MODEL

Consider an L-shaped corner scenario constructed by two rectangular walls, named Wall-1 and Wall-2, as shown in FIGURE 1. The coordinate origin is set in the bottom left of the scenario and marked as "O". Two perpendicular surfaces of the Wall-1, named Surface-1 and Surface-2, are located at $x = x_{s1}$ and $y = y_{s2}$, respectively. The intersection of Surface-1 and Surface-2 is denoted as $C(x_{s1}, y_{s2})$. A surface of Wall-2, denoted by Surface-3, is located at $x = x_{s3}$.

A UWB L-band monostatic radar is placed on the same side of Surface-2 with the coordinates of $R(x_R, y_R)$. Due to the obstruction of Wall-1, the EM wave radiated from the radar cannot reach the area of interest via the LOS path. In this paper, we divide the L-shaped corner scenario into the LOS region and the NLOS region based on the presence and absence of the EM wave LOS propagation path.

When the target is in the NLOS region, the EM wave emitted by the radar can not propagate to the target along the LOS propagation path, but often travels to the target via diffraction path and reflection paths. To analyze the EM wave propagation characteristics in L-shaped scenario, we establish the EM wave single-trip propagation model and round-trip propagation model in the following.

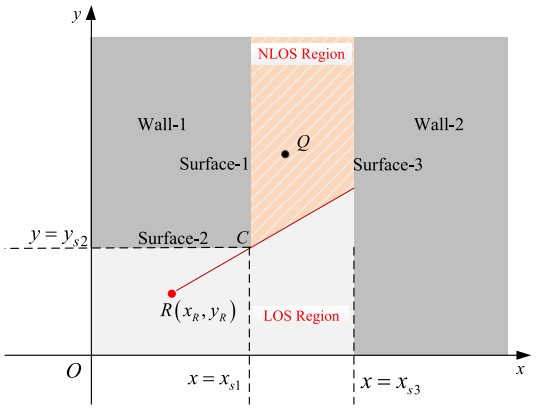

FIGURE 1. L-shaped corner scenario.

A. SINGLE-TRIP PROPAGATION MODEL

To analyze the feasibility of detecting the hidden target in L-shaped scenario, we execute a simulation using the software XFDTD based on the Finite-Difference Time-Domain numerical method. The walls are set homogeneous with the relative permittivity $\varepsilon_w = 4$. The corner C has the position of $(1.5m, 1.5m)$ and the x-coordinate of Surface-3 is $5.0m$. A transmitter antenna is placed at $R\,(0.5m, 0.9m)$ and the receiver is placed at $Q\,(3.0m, 3.0m)$ in the NLOS region. The modulated Gaussian pulse is employed as the probing signal, with center frequency $fc = 1.9$ GHz and bandwidth $B = 600$ MHz. The simulation time is set to 0.08 us.

FIGURE 2 shows the EM wave energy distributions at different simulation times during EM wave propagation. We can observe that EM wave is emitted from the radar antenna R (Fig. 2(a)), part of the EM wave diffracts on C and the other part continues to propagate forward (FIGURE 2(b)). In FIGURE 2(c), the diffraction wave propagates to receiver Q and part of the EM wave reflects on Surface-3. After that, part of the reflection wave reaches receiver Q and the other part propagates forward (FIGURE 2(d)). The EM wave then reflects on Surface-1 (FIGURE 2(e)) and propagates to receiver Q (FIGURE 2(f)). After the reflection on Surface-3 (FIGURE 2(g)), the EM wave at last reaches receiver Q (FIGURE 2(h)).

It can be seen from the above EM wave propagation characteristics that the EM wave can reach the receiver via diffraction path and multi-times reflection paths. For simplicity and without loss of generality, we abstract four single-trip paths from FIGURE 2, as shown in FIGURE 3. Let $\mathcal{P}_i, i \in \{I, II, III, IV\}$ denote the single-trip paths in FIGURE 3. The details of the propagation paths are introduced as follows:

1) $\mathcal{P}_I$(diffraction path): $R \rightarrow C \rightarrow Q$ [seen in FIGURE 3(a)]. The signal radiated from the transmitter

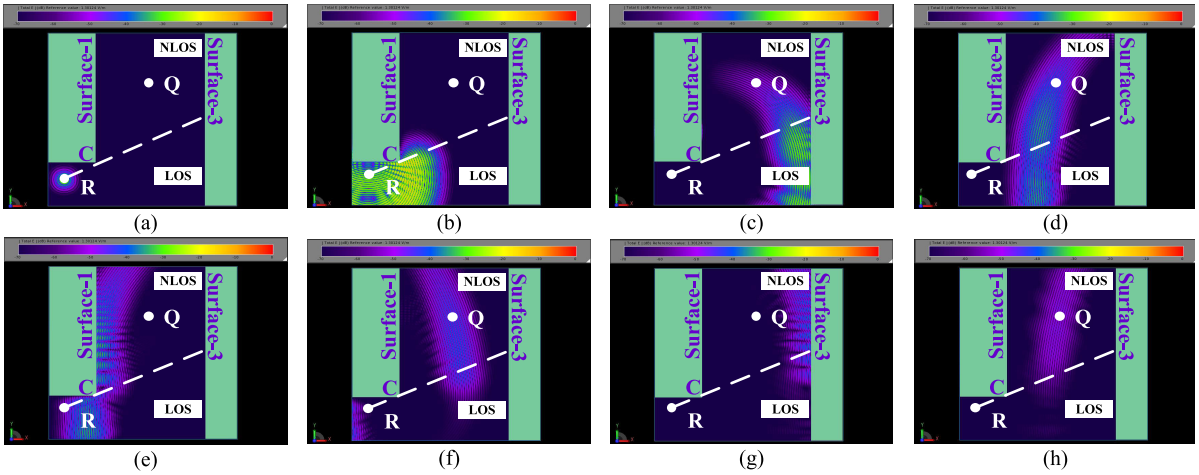

FIGURE 2. EM wave energy distributions at eight different moments, (a)0.005us, (b)0.013us, (c)0.023us, (d)0.033us, (e)0.038us, (f)0.044us, (g)0.050us, (h)0.057us.

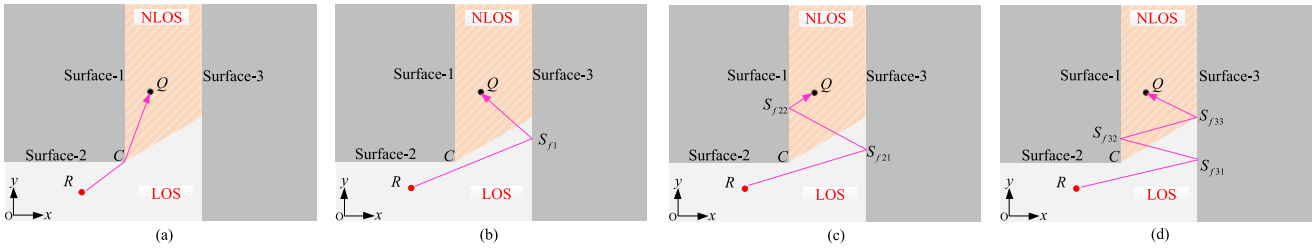

FIGURE 3. Single-trip propagation paths of four different propagation paths, (a)$\mathcal{P}_I$, (b)$\mathcal{P}_{II}$, (c)$\mathcal{P}_{III}$, (d)$\mathcal{P}_{IV}$.

R passed by the diffraction point C and propagates to receiver Q. The corresponding EM wave propagation process is shown in FIGURE 2(a)-(c).

2) $\mathcal{P}_{II}$(once-reflection path) : $R \rightarrow S_{f1} \rightarrow Q$ [seen in FIGURE 3(b)]. The EM wave emitted from transmitter R bounces once on S_{f1} of Surface-3 and propagates to receiver Q via the reflection path. FIGURE 2(a)-(d) show the corresponding EM wave propagation processes.
3) $\mathcal{P}_{III}$ (twice-reflection path): $R \rightarrow S_{f21} \rightarrow S_{f22} \rightarrow Q$ [seen in FIGURE 3(c)]. The signal radiated from transmitter R, passing by the reflection point S_{f21} on Surface-1 and the reflection point S_{f22} on Surface-3, propagates to receiver Q. FIGURE 2(a)-(f) illustrate the corresponding EM wave propagation processes.
4) $\mathcal{P}_{IV}$ (three-times-reflection path):$R \rightarrow S_{f31} \rightarrow S_{f32} \rightarrow S_{f33} \rightarrow Q$ [seen in FIGURE 3(d)]. The signal radiated from the transmitter R, passing by the reflection point S_{f31}, S_{f32} and S_{f33}, propagates to receiver Q. The corresponding EM wave propagations are illustrated in FIGURE 2(a)-(h).

Apart from the above four types of paths, the signal can also propagate to the target via four or more times reflection paths. However, due to the energy attenuation caused by the EM wave reflection, the signal passed by four or more times reflection paths are too weak to be extracted. We thus only consider the above four types of single-trip paths in this paper.

TABLE 1. Lengths of the four single-trip paths.

	$\mathcal{P}_I$	$\mathcal{P}_{II}$	$\mathcal{P}_{III}$	$\mathcal{P}_{IV}$
Theoretical Locations	3.288m	6.831m	9.730m	13.662m
Extracted Locations	3.294m	6.836m	9.746m	13.680m
Error	0.006m	0.005m	0.016m	0.018m

Let $l_i, i \in \{I, II, III, IV\}$ denote the length of $\mathcal{P}_i$. According to the single-trip propagation model of the EM wave, the lengths of $\mathcal{P}_I$, $\mathcal{P}_{II}$, $\mathcal{P}_{III}$, and $\mathcal{P}_{IV}$ can be computed by

$$\begin{cases} l_I = l_{RC} + l_{CQ}, \\ l_{II} = l_{RS_{f1}} + l_{S_{f1}Q} = l_{QR_{II}}, \\ l_{III} = l_{RS_{f21}} + l_{S_{f21}S_{f22}} + l_{S_{f22}Q} = l_{QR_{III}}, \\ l_{IV} = l_{RS_{f31}} + l_{S_{f31}S_{f32}} + l_{S_{f32}S_{f33}} + l_{S_{f33}Q} = l_{QR_{IV}}, \end{cases} \tag{1}$$

where l_{RC} represents the Euclidean distance between points R and C. $R_i, i \in \{II, III, IV\}$ denotes the equivalent radar antenna with respect to $\mathcal{P}_i$. Specifically, R_{II} is the first-order symmetry point of radar R about Surface-3 (see FIGURE 4(a)), R_{III} denotes the second-order symmetry point

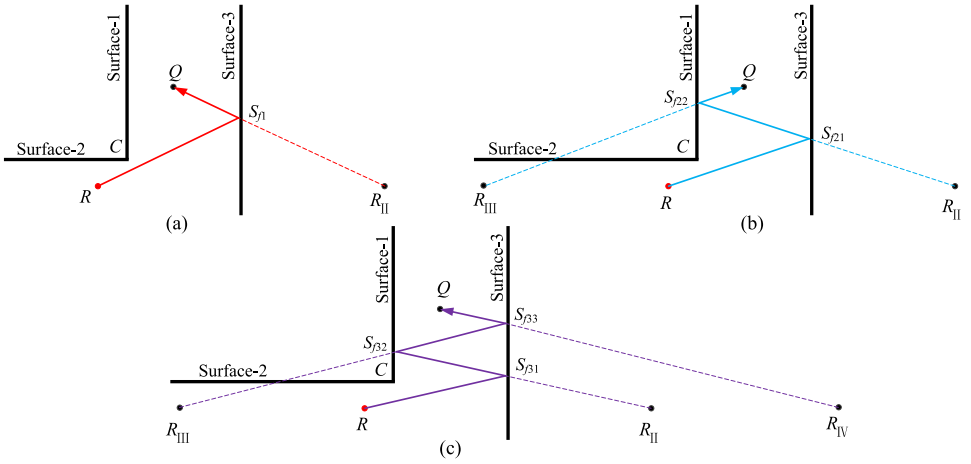

FIGURE 4. Equivalent radar antennas for three different propagation paths, (a)$\mathcal{P}_{II}$, (b)$\mathcal{P}_{III}$, (c)$\mathcal{P}_{IV}$.

of R on Surface-1 and Surface-3. R_{II} and R_{III} are symmetric on Surface-1 (see FIGURE 4(b)). R_{IV} denotes the third-order symmetry point of R on Surface-1 and Surface-3. R_{IV} and R_{III} are symmetric on Surface-3 (see FIGURE 4(c)). According to the known building layout, the equivalent radar antenna $R_{II}(x_{II}, y_{II})$, $R_{III}(x_{III}, y_{III})$ and $R_{IV}(x_{IV}, y_{IV})$ can be obtained as

$$\begin{cases} x_{II} = 2x_{s3} - x_R, \\ x_{III} = 2x_{s1} - 2x_{s3} + x_R, \\ x_{IV} = 4x_{s3} - 2x_{s1} - x_R, \\ y_{II} = y_{III} = y_{IV} = y_R. \end{cases} \tag{2}$$

To validate the correctness of the single-trip propagation models above, we illustrate the received signal of receiver Q in FIGURE 5. It can be seen that there appear several peaks. To determine whether these peaks are generated by the above single-trip paths, we first calculate the Locations of these single-trip paths using (1) and list the theoretical Locations in TABLE 1. Then, the data cursor in MATLAB is used to extract the positions of the peaks in FIGURE 5 and the extracted locations are listed in TABLE 1. Comparing the theoretical Locations with the extracted locations, we find that these echo peaks are appearing close to the theoretical calculated locations. The maximum error between the extracted locations and the calculated locations is 1.8 cm, which suggests that the four strongest peaks in FIGURE 5 match correctly with $\mathcal{P}_i, i \in \{II, III, IV\}$. Moreover, it is obvious that except for these peaks derived from the above four paths, the amplitudes of other peaks are too weak to be considered in this paper.

B. ROUND-TRIP PROPAGATION MODEL BETWEEN RADAR AND TARGET

In this section, we place the transmitter and the receiver at the same position R and place the target at Q in NLOS region to establish the round-trip propagation model for L-shaped scenario. Since both of the transmitting and receiving signals

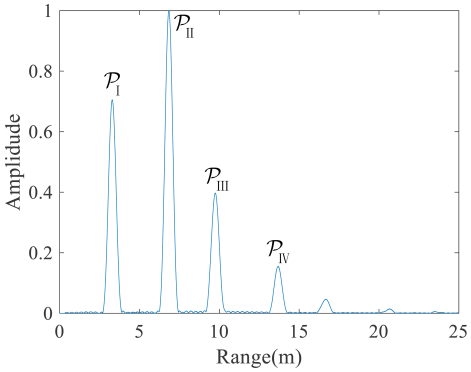

FIGURE 5. Signal received by receiver Q in NLOS region.

may propagate along $\mathcal{P}_i, i \in \{I, II, III, IV\}$, there are sixteen round-trip propagation paths $\mathcal{P}_{i,j}, i, j \in \{I, II, III, IV\}$ between the radar and the target, as shown in TABLE 2.

Because the transmitter and the receiver are at the same location, the round-trip path $\mathcal{P}_{i,j}$ and $\mathcal{P}_{j,i}$ have the same propagation distance when $i, j \in \{I, II, III, IV\}, i \neq j$, which means that there are six equivalent relationships, i.e.

$$\begin{cases} \mathcal{P}_{I,II} \sim \mathcal{P}_{II,I}, \mathcal{P}_{I,III} \sim \mathcal{P}_{III,I}, \mathcal{P}_{I,IV} \sim \mathcal{P}_{IV,I}, \\ \mathcal{P}_{II,III} \sim \mathcal{P}_{III,II}, \mathcal{P}_{II,IV} \sim \mathcal{P}_{IV,II}, \mathcal{P}_{III,IV} \sim \mathcal{P}_{IV,III}. \end{cases} \tag{3}$$

Therefore, only ten round-trip propagation paths are discussed in this paper, as listed in the upper triangular in TABLE 2. The details of the EM wave propagation paths are introduced as follows:

1) $\mathcal{P}_{I,I}$(round-trip diffraction path): the corresponding EM wave propagation path is $R \rightarrow C \rightarrow Q \rightarrow C \rightarrow R$, as shown in FIGURE 6(a). The signal radiated from radar R, passing by the diffraction point C, propagates to target Q and then returns along the same path.
2) $\mathcal{P}_{I,II}$(diffraction path transmitting and once-reflection path receiving): the corresponding EM wave propagation path is $R \rightarrow C \rightarrow Q \rightarrow S_{f1} \rightarrow R$, as shown

TABLE 2. Round-trip propagation paths between radar and target.

Round-Trip Path \ Receive Path / Transmit Path	$\mathcal{P}_I$	$\mathcal{P}_{II}$	$\mathcal{P}_{III}$	$\mathcal{P}_{IV}$
$\mathcal{P}_I$	$\mathcal{P}_{I,I}$	$\mathcal{P}_{I,II}$	$\mathcal{P}_{I,III}$	$\mathcal{P}_{I,IV}$
$\mathcal{P}_{II}$	$\mathcal{P}_{II,I}$	$\mathcal{P}_{II,II}$	$\mathcal{P}_{II,III}$	$\mathcal{P}_{II,IV}$
$\mathcal{P}_{III}$	$\mathcal{P}_{III,I}$	$\mathcal{P}_{III,II}$	$\mathcal{P}_{III,III}$	$\mathcal{P}_{III,IV}$
$\mathcal{P}_{IV}$	$\mathcal{P}_{IV,I}$	$\mathcal{P}_{IV,II}$	$\mathcal{P}_{IV,III}$	$\mathcal{P}_{IV,IV}$

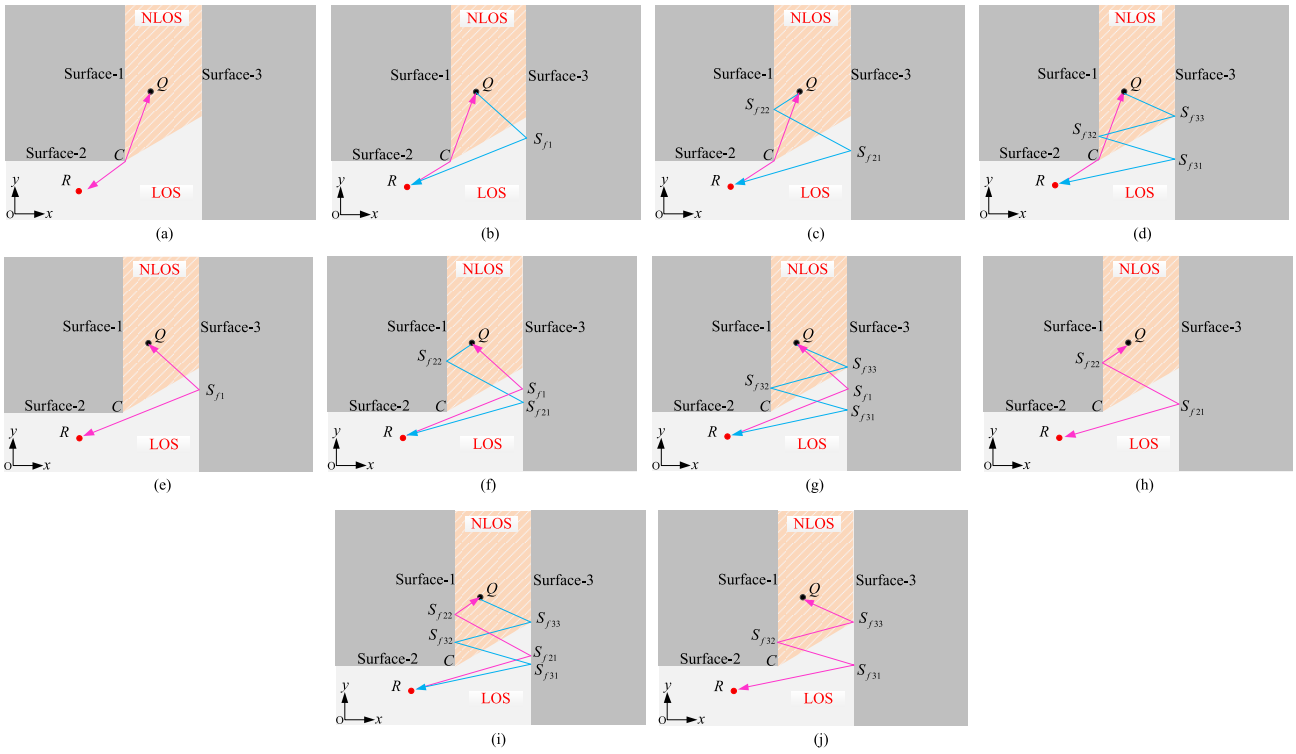

FIGURE 6. The EM wave propagation models, (a)$\mathcal{P}_{I,I}$, (b)$\mathcal{P}_{I,II}$, (c)$\mathcal{P}_{I,III}$, (d)$\mathcal{P}_{I,IV}$, (e)$\mathcal{P}_{II,II}$, (f)$\mathcal{P}_{II,III}$, (g)$\mathcal{P}_{II,IV}$, (h)$\mathcal{P}_{III,III}$, (i)$\mathcal{P}_{III,IV}$, (j)$\mathcal{P}_{IV,IV}$.

in FIGURE 6(b). The signal transmits to the target Q via the diffraction path and then returns to the radar R via the reflection path which bounces once on S_{f1} of Surface-3.

3) $\mathcal{P}_{I,III}$(diffraction path transmitting and twice-reflection path receiving): the EM wave propagates along the path $R \rightarrow C \rightarrow Q \rightarrow S_{f22} \rightarrow S_{f21} \rightarrow R$, as shown in FIGURE 6(c). The transmitting signal, passing by the diffraction path, propagates to target Q and returns to radar R along the twice-reflection path.
4) $\mathcal{P}_{I,IV}$(diffraction path transmitting and three-times-reflection path receiving): the signal propagates along the path $R \rightarrow C \rightarrow Q \rightarrow S_{f33} \rightarrow S_{f32} \rightarrow S_{f31} \rightarrow R$, as shown in FIGURE 6(d). The signal radiated from radar R, passing by the diffraction point C, propagates to target Q and then returns to R passing by the reflection point S_{f31}, S_{f33} of Surface-3 and S_{f32} of Surface-2.
5) $\mathcal{P}_{II,II}$(round-trip once-reflection path): the corresponding EM wave propagation path is $R \rightarrow S_{f1} \rightarrow Q \rightarrow S_{f1} \rightarrow R$, as shown in FIGURE 6(e). The signal transmits to target Q via the once-reflection path and then returns to R along the same path.
6) $\mathcal{P}_{II,III}$(once-reflection path transmitting and twice-reflection path receiving): the EM wave propagates along the path $R \rightarrow S_{f1} \rightarrow Q \rightarrow S_{f22} \rightarrow S_{f21} \rightarrow R$, as shown in FIGURE 6(f). The transmitting signal propagates to target Q via the once-reflection path and propagates back to R along the twice-reflection path.

TABLE 3. Lengths of the round-trip paths.

	$\mathcal{P}_{I,I}$	$\mathcal{P}_{I,II}$	$\mathcal{P}_{I,III}$	$\mathcal{P}_{I,IV}$	$\mathcal{P}_{II,II}$	$\mathcal{P}_{II,III}$	$\mathcal{P}_{II,IV}$	$\mathcal{P}_{III,III}$	$\mathcal{P}_{III,IV}$	$\mathcal{P}_{IV,IV}$
Theoretical Locations	7.785m	10.410m	14.238m	17.187m	13.038m	16.866m	19.814m	20.699m	23.647m	26.597m
Extracted Locations	7.780m	10.426m	14.230m	17.195m	13.031m	16.880m	19.829m	20.712m	23.650m	26.591m
Error	0.005m	0.016m	0.008m	0.005m	0.008m	0.014m	0.015m	0.013m	0.003m	0.006m

TABLE 4. The summary of L-band EM wave propagation paths in an L-shaped corner scenario.

Transmit Path	$\mathcal{P}_{I}$	$\mathcal{P}_{II}$	$\mathcal{P}_{III}$	$\mathcal{P}_{IV}$						
Receive Path	$\mathcal{P}_{I}$	$\mathcal{P}_{II}$	$\mathcal{P}_{III}$	$\mathcal{P}_{IV}$						
Round-trip Path	$\mathcal{P}_{I,I}$	$\mathcal{P}_{I,II}$	$\mathcal{P}_{I,III}$	$\mathcal{P}_{I,III}$	$\mathcal{P}_{II,II}$	$\mathcal{P}_{II,III}$	$\mathcal{P}_{II,IV}$	$\mathcal{P}_{III,III}$	$\mathcal{P}_{III,IV}$	$\mathcal{P}_{IV,IV}$

7) $\mathcal{P}_{II,IV}$(once-reflection path transmitting and three-times-reflection path receiving): the EM wave propagates along the path $R \rightarrow S_{f1} \rightarrow Q \rightarrow S_{f33} \rightarrow S_{f32} \rightarrow S_{f31} \rightarrow R$, as shown in FIGURE 6(g). The signal radiated from radar R propagates to target Q passing by the reflection point S_{f1} of Surface-3 and then returns to R passing by the reflection point S_{f31}, S_{f33} of Surface-3 and S_{f32} of Surface-2.
8) $\mathcal{P}_{III,III}$(round-trip twice-reflection path): the EM wave propagates along the path $R \rightarrow S_{f21} \rightarrow S_{f22} \rightarrow Q \rightarrow S_{f22} \rightarrow S_{f21} \rightarrow R$, as shown in FIGURE 6(h). The signal transmits to target Q via the twice-reflection path and then returns to R passing by the same path.
9) $\mathcal{P}_{III,IV}$(twice-reflection path transmitting and three-times-reflection path receiving): the corresponding EM wave propagation path is $R \rightarrow S_{f21} \rightarrow S_{f22} \rightarrow Q \rightarrow S_{f33} \rightarrow S_{f32} \rightarrow S_{f31} \rightarrow R$, as shown in FIGURE 6(i). The signal radiated from radar R, passing by the reflection path, propagates to target Q which bounces on S_{f21} of Surface-3 and S_{f22} of Surface-1 and then returns to R passing by the reflection point S_{f31}, S_{f33} of Surface-3 and S_{f32} of Surface-2.
10) $\mathcal{P}_{IV,IV}$(round-trip three-times-reflection path): the EM wave propagates along the path $R \rightarrow S_{f31} \rightarrow S_{f32} \rightarrow S_{f33} \rightarrow Q \rightarrow S_{f33} \rightarrow S_{f32} \rightarrow S_{f31} \rightarrow R$, as shown in FIGURE 6(j). The signal propagates to the target by the three-times-reflection path and returns via the same path.

Let $l_{i,j}, i, j \in \{I, II, III, IV\}$ denote the length of $\mathcal{P}_{i,j}$, then, based on the above round-trip propagation model, $l_{i,j}$ can be computed via Eq.(4), as shown at the bottom of the next page.

To verify the EM wave round-trip propagation model, we simulate a single moving target that moves along a curve track by FDTD-based software. The simulation scenario is shown in FIGURE 7. The walls are homogeneous with the relative permittivity $\varepsilon_w = 4$. The corner C has the

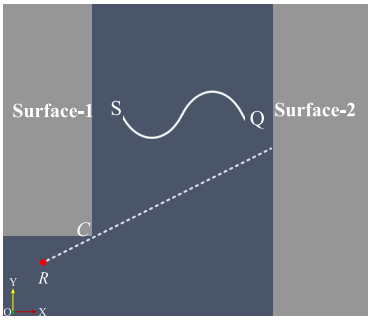

FIGURE 7. EM Simulation scenario of a moving target that moves along a curve route.

coordinates of $(1.5m, 1.5m)$ and the x-coordinate of Surface-3 is 5.0m. The radar is located at $R\,(0.5m, 0.9m)$. A single target moves from $S\,(2.12m, 2.6m)$ to $Q\,(4.0m, 2.8m)$ along a curve route.

FIGURE 8 shows the EM simulation results of the moving target. It can be seen from FIGURE 8(a) that there are several range tracks. Because the target motion trajectory is continuous, we only need to distinguish the echoes of one period to determine whether these range tracks are generated by the above round-trip paths. TABLE 3 first lists the theoretical Locations of the round-trip paths which are computed by (4), then lists the locations of the peaks corresponding to the 80th period(see FIGURE 8(b)). It is obvious that the maximum error between the extracted locations and the theoretical Locations is only 1.6 cm, which validates the correctness of the proposed round-trip propagation model.

In summary, the L-band EM wave propagation model in an L-shaped corner scenario is shown in TABLE 4. Based on the above analysis, we have

i. The signal which propagates to the target by diffraction and multi-times reflections on surrounding surfaces can be exploited to detect the hidden target.

ii. The signal propagating to the target along four or more times reflections on surrounding surfaces attenuates severely

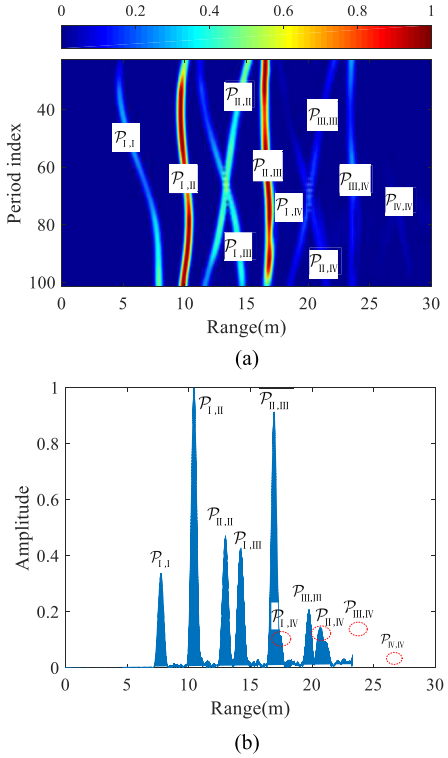

FIGURE 8. Simulation results of single moving target. (a) Range profile plane, (b) echo of the 80th period.

and can be omitted. We therefore only apply four types of single-trip propagation paths (see Subsection A) and ten types of round-trip propagation paths (see Subsection B) to detect the hidden target.

III. MODEL-BASED TARGET LOCALIZATION

In this section, we introduce the target localization algorithm. The signal model is first established based on the EM wave propagation model. Afterwards, we introduce the target location method with the assumption that the multipath types of two TOAs of the returns are known. At last, a TOAs association method is proposed to determine the multipath types of the extracted TOAs.

A. SIGNAL MODEL

Let $s(t)$ denote the transmitted signal. The returns received by the receiver can thus be expressed as

$$y(t) = \sum_{i,j\in\{I,II,III,IV\},i\leq j} \Gamma_{i,j} s\left(t-\tau_{i,j}\right) + d(t) + \xi(t), \quad (5)$$

where $\tau_{i,j}$ denotes the propagation time delay of round-trip path $\mathcal{P}_{i,j}$, $\Gamma_{i,j}$ is the corresponding backscattering coefficient, $d(t)$ is the received direct-coupled signal by the receiver from the transmitter which summarizes the clutters caused by strong reflections from the exterior wall, and $\xi(t)$ denotes the noise.

According to the EM wave propagation model, the propagation time delay $\tau_{i,j}$ can be obtained

$$\tau_{i,j} = \frac{l_{i,j}}{v_c}, i,j \in \{I, II, III, IV\}, i \leq j, \quad (6)$$

where v_c represents the velocity of EM wave in the air and $l_{i,j}$ can be calculated by (4).

B. TARGET LOCATION WITH KNOWN TOAS

Note that if the propagation types of any two TOAs are known, the location of the target can be acquired. In this subsection, we introduce the target location method with the assumption that the propagation types of two multipath returns are known. Based on the proposed EM wave propagation model, the target localization procedure contains two steps, i.e. multipath loci determination and target coordinates calculation.

1) MULTIPATH LOCI DETERMINATION

This step determines the loci of multipaths at the location of the target. According to the types of transmit and receive paths, we divide these round-trip paths into two groups, named as the "*Circle*" group and the "*Ellipse*" group, respectively. Specifically, for each round-trip path in "*Circle*" group, the type of one-trip transmit path is the same as that of the receive path. Thus, the corresponding locus of multipath is a circle [27]. On the contrary, for each round-trip path in "*Ellipse*" group, the type of one-trip transmit path is different from that of one-trip receive path, which leads to the

$$\begin{cases} l_{I,I} = 2l_{RC} + 2l_{QC}, \\ l_{I,II} = l_{RC} + l_{QC} + l_{RS_{f1}} + l_{S_{f1}Q} = l_{RC} + l_{QC} + l_{QR_{II}}, \\ l_{I,III} = l_{RC} + l_{QC} + l_{RS_{f21}} + l_{S_{f21}S_{f22}} + l_{S_{f22}Q} = l_{RC} + l_{QC} + l_{QR_{III}}, \\ l_{I,IV} = l_{RC} + l_{QC} + l_{RS_{f31}} + l_{S_{f31}S_{f32}} + l_{S_{f32}S_{f33}} + l_{S_{f33}Q} = l_{RC} + l_{QC} + l_{QR_{IV}}, \\ l_{II,II} = 2l_{RS_{f1}} + 2l_{S_{f1}Q} = 2l_{QR_{II}}, \\ l_{II,III} = l_{RS_{f1}} + l_{S_{f1}Q} + l_{RS_{f21}} + l_{S_{f21}S_{f22}} + l_{S_{f22}Q} = l_{QR_{II}} + l_{QR_{III}}, \\ l_{II,IV} = l_{RS_{f1}} + l_{S_{f1}Q} + l_{RS_{f31}} + l_{S_{f31}S_{f32}} + l_{S_{f32}S_{f33}} + l_{S_{f33}Q} = l_{QR_{III}} + l_{QR_{IV}}, \\ l_{III,III} = 2l_{RS_{f21}} + 2l_{S_{f21}S_{f22}} + 2l_{S_{f22}Q} = 2l_{QR_{III}}, \\ l_{III,IV} = l_{RS_{f21}} + l_{S_{f21}S_{f22}} + l_{S_{f22}Q} + l_{RS_{f31}} + l_{S_{f31}S_{f32}} + l_{S_{f32}S_{f33}} + l_{S_{f33}Q} = l_{QR_{III}} + l_{QR_{IV}}, \\ l_{IV,IV} = 2l_{RS_{f31}} + 2l_{S_{f31}S_{f32}} + 2l_{S_{f32}S_{f33}} + 2l_{S_{f33}Q} = 2l_{QR_{IV}}. \end{cases} \quad (4)$$

multipath locus following an ellipse [27]. The expressions of these two groups of loci will be introduced in the following.

Theorem 1: The locus equation of multipath corresponds to the round-trip path in "*Circle*" group

Assume that the positions of the equivalent radar antennas for four different one-trip paths have been obtained using (2) and denoted as $R_i(x_i, y_i)$, $i \in \{I, II, III, IV\}$. Then, the locus equation of the multipath corresponds to $\mathcal{P}_{i,i}$, $i \in \{I, II, III, IV\}$, can be expressed as

$$(x - x_i)^2 + (y - y_i)^2 = r_{i,i}^2, \tag{7}$$

where $r_{i,i}$ denotes the propagation path length of $\mathcal{P}_{i,i}$, which is illustrated in Appendix A.

Proof: See Appendix A. ■

Theorem 2: The locus equation of multipath corresponds to the round-trip path in "*Ellipse*" group.

Assume that the positions of these equivalent radar antennas concerning different transmitting and receiving paths have been obtained using (2), which are denoted as $R_i(x_i, y_i)$ and $R_j(x_j, y_j)$, respectively, $i, j \in \{I, II, III, IV\}$, $i < j$. Then the locus equation of multipath corresponds to $\mathcal{P}_{i,j}$ can be expressed as

$$\frac{X^2}{a^2} + \frac{Y^2}{b^2} = 1, \tag{8}$$

where

$$X = x\cos\beta + y\sin\beta - x_{o'}, \tag{9}$$

$$Y = -x\sin\beta + y\cos\beta - y_{o'}, \tag{10}$$

$$\beta = \arccos\frac{x_j - x_{o'}}{c}, \tag{11}$$

$$x_{o'} = \frac{x_i + x_j}{2}, y_{o'} = \frac{y_i + y_j}{2}, \tag{12}$$

$$a = \frac{r_{i,j}}{2}, \tag{13}$$

$$c = \frac{\sqrt{(x_i - x_j)^2 + (y_i - y_j)^2}}{2}, \tag{14}$$

$$b^2 = a^2 - c^2, \tag{15}$$

while $r_{i,j}$ denotes the propagation path length of $\mathcal{P}_{i,j}$, as illustrated in Appendix B.

Proof: See Appendix B. ■

2) TARGET COORDINATES CALCULATION

In the last part, we have obtained the locus equations of two different kinds of multipaths. In this part, we introduce the proposed target localization method considering three different cases. The first case obtains the target location by solving the intersection of any two different "*Circle*" loci while in the second case the location of target can be acquired by solving the intersection of a "*Circle*" locus and an "*Ellipse*" locus. Meanwhile, the third case focuses on the target localization via obtaining the intersection of any two "*Ellipse*" loci. Specifically, these three different cases will be illustrated in Theorem 3, Theorem 4 and Theorem 5, respectively.

Theorem 3: Target localization by two "*Circle*" loci.

Assume that the positions of two equivalent radar antennas for two different EM wave one-trip propagation paths have been obtained using (2), which are denoted as $R_i(x_i, y_i)$ and $R_{i'}(x_{i'}, y_{i'})$, respectively, $i, i' \in \{I, II, III, IV\}$ and $i \neq i'$. Then, the coordinates (x_{tar}, y_{tar}) of the target can be calculated as

$$\begin{cases} x_{tar} = x_i + \dfrac{r_{i,i}\left(-b \pm \sqrt{\Delta}\right)}{2a}, \\ y_{tar} = y_i \pm \dfrac{r_{i,i}\sqrt{4a^2 - b^2 + \Delta \pm 2b\sqrt{\Delta}}}{2a}, \end{cases} \tag{16}$$

with the restrictions of

$$\begin{cases} x_{s1} \leq x_{tar} \leq x_{s3}, \\ y_{s2} \leq y_{tar} \leq y_{\max}, \end{cases} \tag{17}$$

where y_{max} is the maximum y-ordinate of the scenario, a, b and Δ are illustrated in Appendix C.

Proof: See Appendix C. ■

Theorem 4: Target localization by a "*Circle*" locus and an "*Ellipse*" locus

Suppose that the position of the equivalent radar antenna to the "*Circle*" locus has the position of $R_i(x_i, y_i)$. The coordinates of these two equivalent radar antennas related to the "*Ellipse*" locus are denoted as $R_{i'}(x_{i'}, y_{i'})$ and $R_{j'}(x_{j'}, y_{j'})$, respectively, $i', j' \in \{I, II, III, IV\}$ and $i' \neq j'$. Then, the coordinates of the target (x_{tar}, y_{tar}) can be computed as

$$\begin{cases} x_{tar} = 2x_i - x_1 + a\mu_3\cos\beta - b\mu_4\sin\beta, \\ y_{tar} = 2y_i - y_1 + a\mu_3\sin\beta - b\mu_4\cos\beta, \end{cases} \tag{18}$$

with the restrictions of

$$\begin{cases} x_{s1} \leq x_{tar} \leq x_{s3}, \\ y_{s2} \leq y_{tar} \leq y_{\max}, \\ (m_1\mu_3 + n_1\mu_4 + q_1)^2 + (m_2\mu_3 + n_2\mu_4 + q_2)^2 = 1, \\ {\mu_3}^2 + {\mu_4}^2 = 1, \end{cases} \tag{19}$$

where x_1, y_1, a, b, μ_3, μ_4, β, m_1, n_1, q_1, m_1, n_1, q_1 are described in Appendix D.

Proof: See Appendix D. ■

Theorem 5: Target localization by two "*Ellipse*" loci

Assume that the positions of four equivalent radar antennas concerning two different "*Ellipse*" loci have been obtained and denoted as $R_i(x_i, y_i)$, $R_i(x_j, y_j)$, $R_{i'}(x_{i'}, y_{i'})$ and $R_{j'}(x_{j'}, y_{j'})$, respectively, $i, j, i', j' \in \{I, II, III, IV\}$. Then, the coordinates of the target (x_{tar}, y_{tar}) can be expressed as

$$\begin{cases} x_{tar} = a_1\cos\beta_1\mu_1 - b_1\sin\beta_1\mu_2 + x_1, \\ y_{tar} = a_1\sin\beta_1\mu_1 + b_1\cos\beta_1\mu_2 + y_1, \end{cases} \tag{20}$$

with the restrictions of

$$\begin{cases} x_{s1} \leq x_{tar} \leq x_{s3}, \\ y_{s2} \leq y_{tar} \leq y_{\max}, \\ {\mu_1}^2 + {\mu_2}^2 = 1, \\ (m_1\mu_1 + n_1\mu_2 + q_1)^2 + (m_2\mu_1 + n_2\mu_2 + q_2)^2 = 1, \end{cases} \tag{21}$$

where $x_1, y_1, x_2, y_2, a_1, b_1, a_2, b_2, \mu_1, \mu_2, \beta_1, \beta_2, m_1, n_1, q_1, m_1, n_1$, and q_1 are illustrated in Appendix E.

Proof: See Appendix E. ■

C. MODEL-BASED TOAS ASSOCIATION

From the analysis in the previous section, we know that the target location can be obtained by the two known TOAs derived from round-trip paths. However, the multipath types of the TOAs are difficult to identify because that the relative positions and amplitudes of the TOAs vary with the target position. To tackle this problem, we introduce a TOAs association method to recognize the corresponding propagation path type of the extracted TOAs and obtain the true position of the target. Details are as follows:

Step-1: By using the MTI technique and cell average constant false alarm rate (CA-CFAR) detector, we extract the TOAs of the measured signal and then stack these TOAs into a vector $\boldsymbol{T}$, i.e.,

$$\boldsymbol{T} = [\tau_1, \tau_2, \tau_3, \ldots, \tau_K]^T, \tag{22}$$

where K is the total number of the extracted TOAs.

Step-2: The two strongest TOAs in $\boldsymbol{T}$ are chosen to be recognized, denoted as $\tau_{max,1}$ and $\tau_{max,2}$.

Step-3: Since $\tau_{max,1}$ and $\tau_{max,2}$ can be derived by the aforementioned ten types of round-trip paths, there are totally $M = A_{10}^2$ types of combinations for $\tau_{max,1}$ and $\tau_{max,2}$.

Step-4: For the mth combination, suppose that $\tau_{max,1}$ is associated with the round-trip path $\mathcal{P}_{i,j}$, $i, j \in \{I, II, III, IV\}, i \leq j$, and $\tau_{max,2}$ is associated with the round-trip path $\mathcal{P}_{i',j'}$, $i', j' \in \{I, II, III, IV\}, i' \leq j'$. Then, by exploiting the NLOS target localization method mentioned previously, the target candidate can be obtained, denoted as $Q_{candi}^{(m)}$.

Step-5: To evaluate the similarity between the target candidate and the real target, we first calculate all the virtual TOAs $\tau_{i,j}^{(m)}$ of the target candidate $Q_{candi}^{(m)}$ by (6) and then stack all these TOAs in a vector $\boldsymbol{T}_{candi}^{(m)}$, i.e.,

$$\boldsymbol{T}_{candi}^{(m)} = \left[\tau_{I,I}^{(m)}, \tau_{I,II}^{(m)}, \tau_{i,j}^{(m)}, \ldots, \tau_{IV,IV}^{(m)}\right]^T. \tag{23}$$

Afterwards, we define two associating-factors, $N^{(m)}$ and $E^{(m)}$, based on the relevance of vector $\boldsymbol{T}_{candi}^{(m)}$ and vector $\boldsymbol{T}$, which are applied to determine the real target location. Herein, we have

$$N^{(m)} = \sum_{i,j \in \{1,2,3,4\}, i \leq j} f_1\left(\min_{\tau \in \boldsymbol{T}} \left|\tau_{i,j}^{(m)} - \tau\right|\right), \tag{24}$$

and

$$E^{(m)} = \sum_{i,j \in \{1,2,3,4\}, i \leq j} f_2\left(\min_{\tau \in \boldsymbol{T}} \left|\tau_{i,j}^{(m)} - \tau\right|\right), \tag{25}$$

where $|\cdot|$ is the absolute value operator, $f_1(\cdot)$ and $f_2(\cdot)$ are defined as

$$f_1(x) = \begin{cases} 1, & x \leq T_b, \\ 0, & x > T_b, \end{cases} \tag{26}$$

and

$$f_2(x) = \begin{cases} x, & x \leq T_b, \\ 0, & x > T_b, \end{cases} \tag{27}$$

where T_b is a heuristic threshold with small value.

Step-6: Repeat Step-4 and Step-5, we can calculate the corresponding associating-factors of each target candidate $Q_{candi}^{(m)}$, $m = 1, 2, 3, \ldots, M$. Stacking these associating-factors into two vectors $\boldsymbol{N}$ and $\boldsymbol{E}$, then we have

$$\boldsymbol{N} = \left[N^{(1)}, N^{(2)}, N^{(m)}, \ldots, N^{(M)}\right]^T, \tag{28}$$

and

$$\boldsymbol{E} = \left[E^{(1)}, E^{(2)}, E^{(m)}, \ldots, E^{(M)}\right]^T. \tag{29}$$

Note that $N^{(m)}$ represents the number of virtual TOAs of the target candidate $Q_{candi}^{(m)}$ which are matched with the extracted TOAs in $\boldsymbol{T}$ correctly, and $E^{(m)}$ is the corresponding error. In general, if the target candidate $Q_{candi}^{(m)}$ is the true target, $N^{(m)}$ will have the maximum value and $E^{(m)}$ will have the minimum value compared to other candidate targets.

Thus, we identify the target candidate by the following decision rules:

1) Rule-1: If only one element in $\boldsymbol{N}$ is equal to the maximum value of $\boldsymbol{N}$, then, the corresponding target candidate $Q_{candi}^{(m)}$ is chosen as the real target.
2) Rule-2: If several elements in $\boldsymbol{N}$ are equal to the maximum value of $\boldsymbol{N}$, we compare the corresponding elements in $\boldsymbol{E}$ and find the minimum value, the corresponding target candidate $Q_{candi}^{(m)}$ of which is chosen as the real target.

IV. NUMERICAL RESULTS

In this section, simulations and experiments are implemented to validate the effectiveness and robustness of the proposed target localization method.

A. EM SIMULATION RESULTS

The simulation scenario is shown in FIGURE 7 and the range profile is illustrated in FIGURE 8(a). Therein, we can see that several range tracks derived from different round-trip paths. The relative positions and the amplitudes of these range tracks varying with the target locations.

The localization results of the proposed method is depicted in FIGURE 9. It can be seen that most of the targets positions are closed to the ground truth. In FIGURE 10, we give the localization error curve to show the mean square error (MSE) between the ground truth and the extracted position in each period. Note that although the localization error fluctuates in different periods, the maximum MSE is only 6.24cm, which validates the effectiveness of the proposed algorithm.

To analyze the robustness of the developed location method at different noise levels, the recorded data are corrupted with additive white Gaussian noise by assuming the signal-noise-ratio (SNR) of 8 dB to 16 dB. FIGURE 11 shows the error

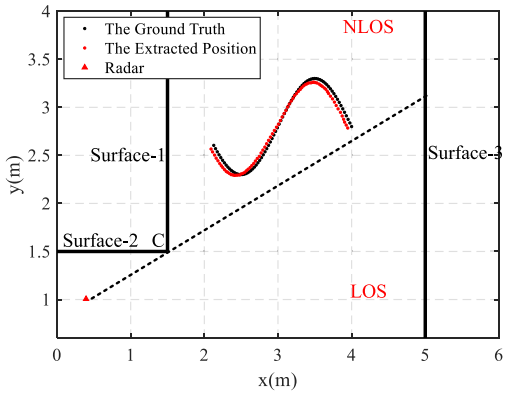

FIGURE 9. Localization results in the simulation scenario.

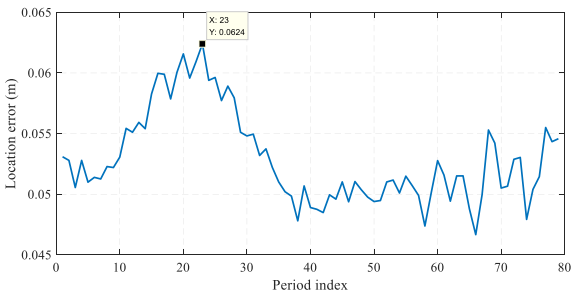

FIGURE 10. Localization error curve in the simulation scenario with no noise.

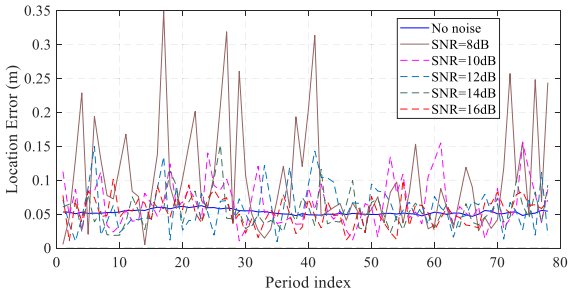

FIGURE 11. Localization error curves at different noise levels.

curves at different noise levels. As we can see, when the SNR is 8 dB, the maximum location error is 35 cm and the location errors are below 20 cm in most periods. Then, when the SNRs are greater than 10 dB, the location errors are below 15 cm steadily, which means that the proposed localization algorithm is robust in these situations.

B. EXPERIMENTAL RESULTS

Several experiments in two different real scenarios have been conducted to prove the effectiveness of the proposed algorithm. The first scenario is shown in FIGURE 12, the corner is located at (*2.0m,2.0m*) and Surface-3 is located at $x = 4.32$ m. A UWB radar with one transmitting and one receiving antenna is placed at the side of Surface-2 to collect the experiment data of the hidden target in NLOS region. The transmitter is located at (1.44*m*, 1.68*m*) and the receiver

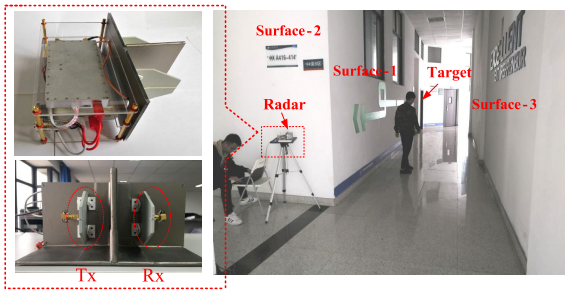

FIGURE 12. The first experimental scenario.

TABLE 5. Parameters of the probing signal.

Parameter	Value
Start frequency	1.6GHz
End frequency	2.2GHz
Bandwidth	600MHz
Number of steps	300
Step frequency	2MHz

FIGURE 13. The second experimental scenario.

is located at (1.47*m*, 1.61*m*), respectively. The stepped frequency continuous waveform [28] is employed as the probing signal and the detailed signal parameters are given in TABLE 5.

By exploiting the UWB radar system aforementioned, two experiments are conducted to obtain the positions of the NLOS target that hides behind the building corner. In the first experiment, the human target sways back and forth within a short range. And in the second experiment there is a single target moving along a straight line. Experimental results are introduced in Case-1 and Case-2 as below.

The second scenario is shown in FIGURE 13, the corner is located at (*2.0m,2.0m*) and Surface-3 is located at $x = 6.36$ m. The transmitter is located at (1.74*m*, 1.72*m*) and the receiver is located at (1.77*m*, 1.64*m*), respectively. The radar system is the same as the first scenario. A single target moves along a straight line in this scenario and the results are introduced in Case-3 as below.

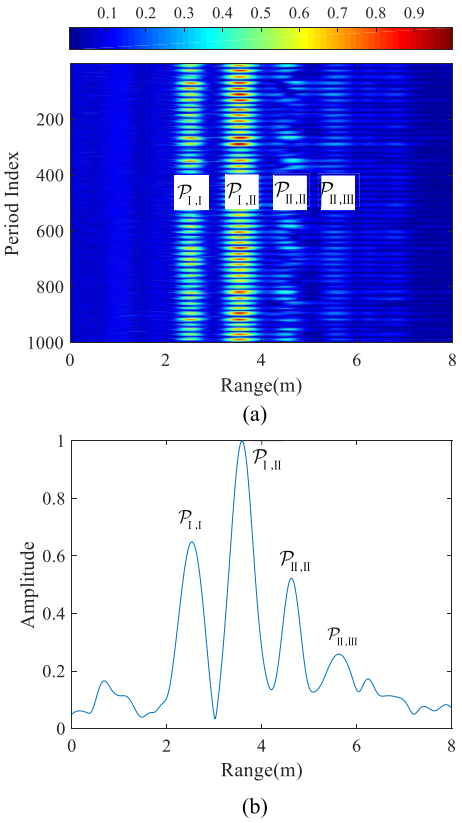

FIGURE 14. Experimental results of micro-motion target, (a)Range profile, (b)echo of the 100th period.

1) CASE-1: MICRO-MOTION TARGET IN THE FIRST SCENARIO

In the first experiment, a person at first stands at the position of (*3.13m,3.54m*). Then, he is swaying back and forth with a small range during the data collection process. The corresponding target range profile is illustrated in FIGURE 14(a) from which we can observe that several range tracks of the micro-motion target are presented. The true multipath types of these range tracks have been marked out. In real experiment, since the human body is not an ideal point target and the surface of the surrounding walls are not completely smooth, the corresponding range tracks expand to a certain extent. Besides, compared with the case of simulation, the signal attenuation is more severe in the experiment due to the clutter. Thus, less range peaks are appearing in FIGURE 14 than the EM simulation.

The target location is obtained by the model-based target localization method, as shown in FIGURE 15. It can be seen that the locations of the target are presented. The average coordinates of the extracted target locations are (*3.0074m,3.6054m*). In the same way as in the simulation, we obtain the maximum MSE between the ground truth position of the target and the average coordinates of the extracted target locations, i.e. 0.14 m. Considering the size of the human body, the error value is within the acceptable range, which validates the effectiveness of the proposed algorithm.

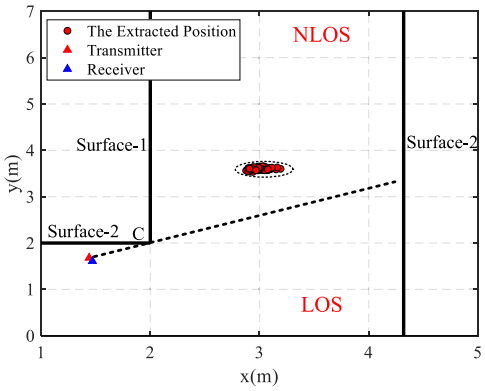

FIGURE 15. Localization results of micro-motion target.

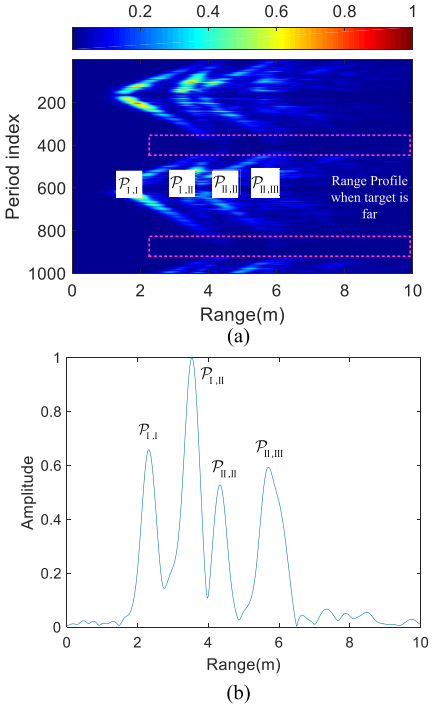

FIGURE 16. Experiment results of single moving target, (a)Range profile, (b)echo of the 100th period.

2) CASE-2: MOVING TARGET IN THE FIRST SCENARIO

In this experiment, a person moves along a straight line between (*2.32m,2.57m*) and (*3.82m,5.17m*) in the NLOS region. FIGURE 16(a) shows the range profile for multiple periods of the experiment data and FIGURE 16(b) is the range profile of the 100th period. Therein, we mark out the range tracks of the moving target. For most of the data periods, there are four range trajectories, as shown in FIGURE 16(a). However, for each range trajectory, the amplitude of the echo decreases as the EM propagation range increases. Therefore, when the target is at the farthest position, the amplitude of the echo received is very weak (see the dotted red box in FIGURE 16(a)). In this case, it is difficult to acquire the target location. However, by applying the proposed method and using the Kalman filter to improve the

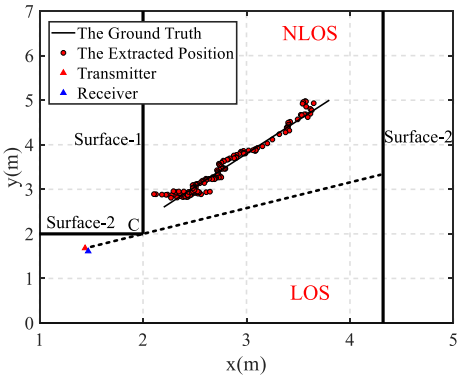

FIGURE 17. Localization results for single moving target.

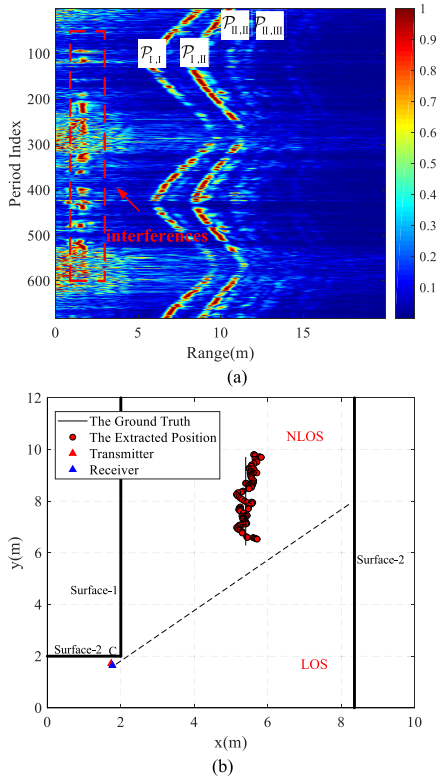

FIGURE 18. Experimental results of the second scenario, (a)Range profile, (b)the localization results.

localization results [29], [30]. The target location result is presented in FIGURE 17. We observe that although there are some missed detections of TOAs in real experiment, the motion of the human target is still clearly presented. Thus, the proposed method is effective in NLOS target positioning.

3) CASE-3: MOVING TARGET IN THE SECOND SCENARIO

In this experiment, a person moves along a straight line between (*5.4m,6.3m*) and (*5.4m,9.7m*) in the NLOS region. FIGURE 18 shows the experimental results of the second scenario. For most of the data periods, there are four range trajectories, as shown in FIGURE 18(a). Also, it can be seen that there exist some interferences when the target is at the farthest position (see the red dotted boxes FIGURE 18(a)). Although there are some non-motor vehicles in the scenario (see from FIGURE 13), which lead to location errors, the target trajectory is obtained by the proposed method accurately.

V. CONCLUSION

This paper addresses a corner target localization problem by using a monostatic L-band UWB radar. We have established an EM wave propagation model by analyzing the characteristics of the measured signal. Based on the established model, a target localization algorithm using a TOAs association method which can match the measured TOAs with the corresponding EM propagation paths correctly have been developed. Numerical results have demonstrated that even with some missed detections of TOAs, the human movement can still be obtained correctly. Possible future work might concern the study of multi-target localization.

VI. PROOF OF THEOREM 1

For the round-trip path $\mathcal{P}_{i,i}$ in the "*Circle*" group, we can obtain the following relationships based on (4), i.e.

$$\begin{aligned} r_{I,I} &= l_{QC}, r_{II,II} = l_{QR_{II}}, \\ r_{III,III} &= l_{QR_{III}}, r_{IV,IV} = l_{QR_{IV}}. \end{aligned} \tag{30}$$

where

$$\begin{cases} r_{I,I} = \dfrac{l_{I,I} - 2l_{RC}}{2} = \dfrac{v_c\tau_{I,I} - 2l_{RC}}{2}, \\ r_{II,II} = \dfrac{l_{II,II}}{2} = \dfrac{v_c\tau_{II,II}}{2}, \\ r_{III,III} = \dfrac{l_{III,III}}{2} = \dfrac{v_c\tau_{III,III}}{2}, \\ r_{IV,IV} = \dfrac{l_{IV,IV}}{2} = \dfrac{v_c\tau_{IV,IV}}{2}. \end{cases} \tag{31}$$

From (22), it is clear that the target locates at two different circle loci. The first circle locus has a center of C and a radius of $r_{I,I}$, while the other circle locus has a center of R_i and a radius of $r_{i,i}$, $i \in \{II, III, IV\}$. For ease of description, we use R_I to represent C in (22). Therefore, the equation of the multipath circle is achieved as

$$(x - x_i)^2 + (y - y_i)^2 = r_{i,i}^2, i \in \{I, II, III, IV\}. \tag{32}$$

VII. PROOF OF THEOREM 2

For the round-trip path $\mathcal{P}_{i,j}$ in the "*Ellipse*" group, $i < j$, we have the following relationships based on (4), i.e.

$$\begin{cases} r_{I,II} = l_{QR_I} + l_{QR_{II}}, r_{I,III} = l_{QR_I} + l_{QR_{III}}, \\ r_{I,IV} = l_{QR_I} + l_{QR_{IV}}, r_{II,III} = l_{QR_{II}} + l_{QR_{III}}, \\ r_{II,IV} = l_{QR_{II}} + l_{QR_{IV}}, r_{III,IV} = l_{QR_{III}} + l_{QR_{IV}}, \end{cases} \tag{33}$$

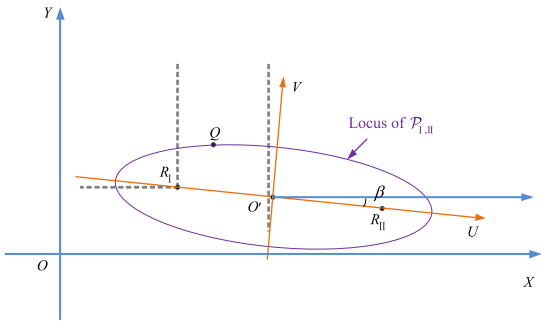

FIGURE 19. The locus of $\mathcal{P}_{I,II}$.

where C has been replaced by R_I and

$$\begin{cases} r_{I,II} = l_{I,II} - l_{RR_I} = v_c\tau_{I,II} - l_{RR_I}, \\ r_{I,III} = l_{I,III} - l_{RR_I} = v_c\tau_{I,III} - l_{RR_I}, \\ r_{I,IV} = l_{I,IV} - l_{RR_I} = v_c\tau_{I,IV} - l_{RR_I}, \\ r_{II,III} = l_{II,III} = v_c\tau_{II,III}, \\ r_{II,IV} = l_{II,IV} = v_c\tau_{II,IV}, \\ r_{III,IV} = l_{III,IV} = v_c\tau_{III,IV}. \end{cases} \tag{34}$$

From (33), it is obvious that the target is on an ellipse locus with two focal points R_i and R_j, and the major axis $r_{i,j}$, $i, j \in \{I, II, III, IV\}$, $i < j$.

To prove Theorem 2, we first introduce the derivation process of round-trip path $\mathcal{P}_{I,II}$. The multipath ellipse locus of $\mathcal{P}_{I,II}$ is illustrated in FIGURE 13 with two focal points $R_I(x_I, y_I)$ and $R_{II}(x_{II}, y_{II})$. In order to obtain the equation of the ellipse, the auxiliary coordinate system $UO'V$ is established, as shown in the orange line of FIGURE 19. The coordinates of O' can be calculated as

$$\begin{cases} x_{o'} = \dfrac{x_I + x_{II}}{2}, \\ y_{o'} = \dfrac{y_I + y_{II}}{2}. \end{cases} \tag{35}$$

Thus, the elliptical standard equation in $UO'V$ coordinate system can be denoted as

$$\frac{u^2}{a^2} + \frac{v^2}{b^2} = 1, \tag{36}$$

where a and b represent the lengths of the semi-major and the semi-minor axis, respectively.

According to the property of ellipse, we get the corresponding parameters as below

$$\begin{cases} a = \dfrac{l_{R_IQ} + l_{R_{II}Q}}{2} = \dfrac{r_{I,II}}{2}, \\ c = \dfrac{l_{R_IR_{II}}}{2} = \dfrac{\sqrt{(x_I - x_{II})^2 + (y_I - y_{II})^2}}{2}, \\ b^2 = a^2 - c^2, \end{cases} \tag{37}$$

where c denotes half of the focal length.

According to the translation and rotation theory of cartesian coordinate system, we get

$$\begin{bmatrix} u \\ v \end{bmatrix} = \begin{bmatrix} \cos\beta & \sin\beta \\ -\sin\beta & \cos\beta \end{bmatrix} \begin{bmatrix} x \\ y \end{bmatrix} - \begin{bmatrix} x_{o'} \\ y_{o'} \end{bmatrix}, \tag{38}$$

where β denotes the angle between the X-axis positive direction and the U-axis positive direction, which can be calculated as

$$\beta = \arccos\frac{x_I - x_{o'}}{c}. \tag{39}$$

Thus, the ellipse equation in XOY coordinate system can be expressed as

$$\frac{X^2}{a^2} + \frac{Y^2}{b^2} = 1, \tag{40}$$

where

$$X = u = x\cos\beta + y\sin\beta - x_{o'}, \tag{41}$$

and

$$Y = v = -x\sin\beta + y\cos\beta - y_{o'}. \tag{42}$$

Following the same idea, we can also achieve the proofs of the other ellipse equations with respect to the remaining round-trip paths $\mathcal{P}_{i,j}$, $i < j$.

VIII. PROOF OF THEOREM 3

Assume that the equations of two multipath circles are obtained by Theorem 1, which are respectively expressed as

$$(x - x_i)^2 + (y - y_i)^2 = r_{i,i}^2, \tag{43}$$

and

$$(x - x_{i'})^2 + (y - y_{i'})^2 = r_{i',i'}^2. \tag{44}$$

By introducing an extra parameter $t \in [0, 2\pi]$, we rewrite the equation of the first circle in (43) as

$$\begin{cases} x = x_i + r_{i,i}\cos t, \\ y = y_i + r_{i,i}\sin t. \end{cases} \tag{45}$$

Substituting (45)) into (44), we have

$$\left(x_i + r_{i,i}\cos t - x_{i'}\right)^2 + \left(y_i + r_{i,i}\sin t - y_{i'}\right)^2 = r_{i',i'}^2. \tag{46}$$

Then, (46) can be transformed to

$$\begin{aligned} 2r_{i,i}\left(x_i - x_{i'}\right)\cos t + 2r_{i',i'}\left(y_i - y_{i'}\right)\sin t \\ = r_{i',i'}^2 - r_{i,i}^2 - (x_i - x_{i'})^2 + (y_i - y_{i'})^2. \end{aligned} \tag{47}$$

To simplify the analysis above, we define the following three parameters:

$$\begin{cases} a = 2r_{i,i}\left(x_i - x_{i'}\right), \\ b = 2r_{i',i'}\left(y_i - y_{i'}\right), \\ c = r_{i',i'}^2 - r_{i,i}^2 - (x_i - x_{i'})^2 + (y_i - y_{i'})^2. \end{cases} \tag{48}$$

Then, (47) can be rewritten as

$$a\cos t + b\sin t = c. \tag{49}$$

Let $\cos t = x'$ and $\sin t = \pm\sqrt{1-x'^2}$, then we have

$$\left(a^2+b^2\right)x'^2 - 2acx' + c^2 - b^2 = 0. \tag{50}$$

By solving (50), we obtain

$$\begin{cases} \cos\theta = x' = \dfrac{-b \pm \sqrt{\Delta}}{2a}, \\ \sin\theta = \pm\sqrt{1-x'^2} = \pm\dfrac{\sqrt{4a^2 - b^2 + \Delta \pm 2b\sqrt{\Delta}}}{2a}, \end{cases} \tag{51}$$

where

$$\Delta = 4a^2c^2 - 4\left(a^2+b^2\right)\left(c^2-b^2\right) = 4b^2\left(1+a^2-c^2\right). \tag{52}$$

Substituting (51) into (45), the coordinates of the target can be obtained

$$\begin{cases} x_{tar} = x_i + \dfrac{r_{i,i}\left(-b \pm \sqrt{\Delta}\right)}{2a}, \\ y_{tar} = y_i \pm \dfrac{r_{i,i}\sqrt{4a^2 - b^2 + \Delta \pm 2b\sqrt{\Delta}}}{2a}. \end{cases} \tag{53}$$

IX. PROOF OF THEOREM 4

Assume that the equation of the multipath circle is computed according to Theorem 1 and the equation of the multipath ellipse is obtained by Theorem 2, which are respectively expressed as

$$(x - x_i)^2 + (y - y_i)^2 = r_{i,i}^2, \tag{54}$$

and

$$\frac{X^2}{a^2} + \frac{Y^2}{b^2} = 1, \tag{55}$$

where

$$\begin{cases} X = x\cos\beta + y\sin\beta - x_{o'}, \\ Y = -x\sin\beta + y\cos\beta - y_{o'}, \\ \beta = \arccos\dfrac{x_{j'} - x_{o'}}{c}, \\ x_{o'} = \dfrac{x_{i'} + x_{j'}}{2}, y_{o'} = \dfrac{y_{i'} + y_{j'}}{2}, \\ a = \dfrac{r_{i',j'}}{2}, \\ c = \dfrac{\sqrt{\left(x_{i'} - x_{j'}\right)^2 + \left(y_{i'} - y_{j'}\right)^2}}{2}, \\ b^2 = a^2 - c^2. \end{cases} \tag{56}$$

By introducing two parameters $t_1, t_2 \in [0, 2\pi]$, (54) and (55) can be rewritten as

$$\begin{cases} x = x_i + r_{i,i}\cos t_1, \\ y = y_i + r_{i,i}\sin t_1, \end{cases} \tag{57}$$

and

$$\begin{cases} x\cos\beta + y\sin\beta - x_{o'} = a\cos t_2, \\ -x\sin\beta + y\cos\beta - y_{o'} = b\sin t_2. \end{cases} \tag{58}$$

Furthermore, (58) can be simplified as

$$\begin{cases} x = a\cos\beta\cos t_2 - b\sin\beta\sin t_2 + x_1, \\ y = a\sin\beta\cos t_2 + b\cos\beta\sin t_2 + y_1, \end{cases} \tag{59}$$

where

$$\begin{cases} x_1 = x_{o'}\cos\beta - y_{o'}\sin\beta, \\ y_1 = x_{o'}\sin\beta - y_{o'}\cos\beta. \end{cases} \tag{60}$$

Thus, we have

$$\begin{cases} x_{tar} = x_i + r_{i,i}\cos t_1 = a\cos\beta\cos t_2 - b\sin\beta\sin t_2 + x_1, \\ y_{tar} = y_i + r_{i,i}\sin t_1 = a\sin\beta\cos t_2 + b\cos\beta\sin t_2 + y_1. \end{cases} \tag{61}$$

To solve (61), we rewrite it into vector form, i.e.

$$c_1 + A_1 t_1 = A_2 t_2 + c_2, \tag{62}$$

where

$$A_1 = \begin{bmatrix} -r_{i,i} & 0 \\ 0 & -r_{i,i} \end{bmatrix}, c_1 = \begin{bmatrix} x_i \\ y_i \end{bmatrix}, t_1 = \begin{bmatrix} \cos t_1 \\ \sin t_1 \end{bmatrix},$$
$$A_2 = \begin{bmatrix} a\cos\beta & -b\sin\beta \\ a\sin\beta & b\cos\beta \end{bmatrix}, c_2 = \begin{bmatrix} x_1 \\ y_1 \end{bmatrix}, t_2 = \begin{bmatrix} \cos t_2 \\ \sin t_2 \end{bmatrix}. \tag{63}$$

Based on (62) and (63), we have

$$[A_1, A_2]\begin{bmatrix} t_1 \\ t_2 \end{bmatrix} = c_2 - c_1. \tag{64}$$

To simplify the analysis, we define

$$A = [A_1, A_2] \in \Re^{2\times 4}, \quad t = \begin{bmatrix} t_1 \\ t_2 \end{bmatrix} \in \Re^{4\times 1}, c = c_2 - c_1 \in \Re^{2\times 1}. \tag{65}$$

Then, (63) can be transformed to

$$At = c. \tag{66}$$

Considering the case that $rank(A) = rank(A, c) = 2 < 4$, the general solution of (66) can be obtained by the generalized inverse of matrix A, named as A^-, i.e.

$$t = A^- c + \left(E_4 - A^- A\right)u, \tag{67}$$

where $(E_4 - A^- A)u$ is the general solution of $At = 0$, E_n is a $n \times n$ identity matrix and u is an arbitrary vector. To calculate the generalized inverse A^-, we calculate the maximum rank decomposition of A. Then, we have

$$A = BD, \tag{68}$$

where

$$\begin{cases} B = \begin{bmatrix} -r_{i,i} & 0 \\ 0 & -r_{i,i} \end{bmatrix}, \\ D = \begin{bmatrix} 1 & 0 & -\dfrac{a}{r_{i,i}}\cos\beta & \dfrac{b}{r_{i,i}}\sin\beta \\ 0 & 1 & -\dfrac{a}{r_{i,i}}\sin\beta & \dfrac{b}{r_{i,i}}\cos\beta \end{bmatrix}. \end{cases} \tag{69}$$

Thus, A^- can be computed by

$$A^- = B_L^{-1} D_R^{-1} = \begin{bmatrix} A_1^{-1} \\ 0_2 \end{bmatrix}, \tag{70}$$

where 0_n is a $n \times n$ zero matrix, B_L^{-1} denotes the left inverse of B and D_R^{-1} is the right inverse of D. The expressions of B_L^{-1} and D_R^{-1} can be expressed as

$$B_L^{-1} = \begin{bmatrix} -\dfrac{1}{r_{i,i}} & 0 \\ 0 & -\dfrac{1}{r_{i,i}} \end{bmatrix}, D_R^{-1} = \begin{bmatrix} 1 & 0 \\ 0 & 1 \\ 0 & 0 \\ 0 & 0 \end{bmatrix}. \tag{71}$$

Therefore, t can be denoted as

$$t = \begin{bmatrix} \cos t_1 \\ \sin t_1 \\ \cos t_2 \\ \sin t_2 \end{bmatrix} = \begin{bmatrix} m_1\mu_3 + n_1\mu_4 + q_1 \\ m_2\mu_3 + n_2\mu_4 + q_2 \\ \mu_3 \\ \mu_4 \end{bmatrix}, \tag{72}$$

where

$$\begin{cases} u = \begin{bmatrix} \mu_1 & \mu_2 & \mu_3 & \mu_4 \end{bmatrix}^T, \\ m_1 = \dfrac{a}{r_{i,i}}\cos\beta, n_1 = -\dfrac{b}{r_{i,i}}\sin\beta, q_1 = \dfrac{1}{r_{i,i}}(x_i - x_1), \\ m_2 = \dfrac{a}{r_{i,i}}\sin\beta, n_1 = \dfrac{b}{r_{i,i}}\cos\beta, q_1 = \dfrac{1}{r_{i,i}}(y_i - y_1). \end{cases} \tag{73}$$

According to trigonometric function relation, we have the following restrictions:

$$\begin{cases} (m_1\mu_3 + n_1\mu_4 + q_1)^2 + (m_2\mu_3 + n_2\mu_4 + q_2)^2 = 1, \\ {\mu_3}^2 + {\mu_4}^2 = 1. \end{cases} \tag{74}$$

Substituting (72) into (61), the coordinates of the target can be obtained and expressed as

$$\begin{cases} x_{tar} = x_i + r_{i,i}\cos t_1 = 2x_i - x_1 + a\mu_3\cos\beta - b\mu_4\sin\beta, \\ y_{tar} = y_i + r_{i,i}\sin t_1 = 2y_i - x_1 + a\mu_3\sin\beta - b\mu_4\cos\beta. \end{cases} \tag{75}$$

X. PROOF OF THEOREM 5

Suppose that the equations of the two multipath ellipses are calculated according to Theorem 2 and expressed as

$$\frac{{X_1}^2}{a_1^2} + \frac{{Y_1}^2}{b_1^2} = 1, \tag{76}$$

and

$$\frac{{X_2}^2}{a_2^2} + \frac{{Y_2}^2}{b_2^2} = 1, \tag{77}$$

where

$$\begin{cases} X_1 = x\cos\beta_1 + y\sin\beta_1 - x_{o'}^{(1)}, \\ Y_1 = -x\sin\beta_1 + y\cos\beta_1 - y_{o'}^{(1)}, \\ X_2 = x\cos\beta_2 + y\sin\beta_2 - x_{o'}^{(2)}, \\ Y_2 = -x\sin\beta_2 + y\cos\beta_2 - y_{o'}^{(2)}, \\ \beta_1 = \arccos\dfrac{x_j - x_{o'}^{(1)}}{c_1}, \\ \beta_2 = \arccos\dfrac{x_{j'} - x_{o'}^{(2)}}{c_2}, \\ x_{o'}^{(1)} = \dfrac{x_i + x_j}{2}, y_{o'}^{(1)} = \dfrac{y_i + y_j}{2}, \\ x_{o'}^{(2)} = \dfrac{x_{i'} + x_{j'}}{2}, y_{o'}^{(2)} = \dfrac{y_{i'} + y_{j'}}{2}, \\ c_1 = \dfrac{\sqrt{(x_i - x_j)^2 + (y_i - y_j)^2}}{2}, \\ c_2 = \dfrac{\sqrt{(x_{i'} - x_{j'})^2 + (y_{i'} - y_{j'})^2}}{2}, \\ a_1 = \dfrac{r_{i,j}}{2}, a_2 = \dfrac{r_{i',j'}}{2}, \\ b_1^2 = a_1^2 - c_1^2, b_2^2 = a_2^2 - c_2^2. \end{cases} \tag{78}$$

By introducing two extra parameters $t_1, t_2 \in [0, 2\pi]$, (76) and (77) can be rewritten as

$$\begin{cases} x = a_1\cos\beta_1\cos t_1 - b_1\sin\beta_1\sin t_1 + x_1, \\ y = a_1\sin\beta_1\cos t_1 + b_1\cos\beta_1\sin t_1 + y_1, \end{cases} \tag{79}$$

and

$$\begin{cases} x = a_2\cos\beta_2\cos t_2 - b_2\sin\beta_2\sin t_2 + x_2, \\ y = a_2\sin\beta_2\cos t_2 + b_2\cos\beta_2\sin t_2 + y_2, \end{cases} \tag{80}$$

where

$$\begin{cases} x_1 = x_{o'}^{(1)}\cos\beta_1 - y_{o'}^{(1)}\sin\beta_1, \\ y_1 = x_{o'}^{(1)}\sin\beta_1 - y_{o'}^{(1)}\cos\beta_1, \end{cases} \tag{81}$$

and

$$\begin{cases} x_2 = x_{o'}^{(2)}\cos\beta_2 - y_{o'}^{(2)}\sin\beta_2, \\ y_2 = x_{o'}^{(2)}\sin\beta_2 - y_{o'}^{(2)}\cos\beta_2. \end{cases} \tag{82}$$

Then, we have

$$\begin{cases} x_{tar} = a_1\cos\beta_1\cos t_1 - b_1\sin\beta_1\sin t_1 + x_1 \\ \quad = a_2\cos\beta_2\cos t_2 - b_2\sin\beta_2\sin t_2 + x_2, \\ y_{tar} = a_1\sin\beta_1\cos t_1 + b_1\cos\beta_1\sin t_1 + y_1 \\ \quad = a_2\sin\beta_2\cos t_2 + b_2\cos\beta_2\sin t_2 + y_2. \end{cases} \tag{83}$$

Transforming (83) into the vector form, we then have

$$A_1 t_1 + c_1 = A_2 t_2 + c_2, \tag{84}$$

where

$$\begin{aligned} A_1 &= \begin{bmatrix} a_1 \cos\beta_1 & -b_1 \sin\beta_1 \\ a_1 \sin\beta & b_1 \cos\beta_1 \end{bmatrix}, \quad c_1 = \begin{bmatrix} x_1 \\ y_1 \end{bmatrix} \\ A_2 &= \begin{bmatrix} -a_1 \cos\beta_1 & b_1 \sin\beta_1 \\ -a_1 \sin\beta & -b_1 \cos\beta_1 \end{bmatrix}, \quad c_2 = \begin{bmatrix} x_2 \\ y_2 \end{bmatrix} \\ t_1 &= \begin{bmatrix} \cos t_1 \\ \sin t_1 \end{bmatrix}, \quad t_2 = \begin{bmatrix} \cos t_2 \\ \sin t_2 \end{bmatrix} \end{aligned} \tag{85}$$

Thus, (84) can be rewritten as

$$[A_1, A_2] \begin{bmatrix} t_1 \\ t_2 \end{bmatrix} = c_2 - c_1. \tag{86}$$

To simplify the analysis, we define

$$A = [A_1, A_2] \in \Re^{2\times 4}, \quad t = \begin{bmatrix} t_1 \\ t_2 \end{bmatrix} \in \Re^{4\times 1}, c = c_2 - c_1 \in \Re^{2\times 1}. \tag{87}$$

Therefore, we have

$$At = c. \tag{88}$$

After conducting the similar process as that of (66))-(72 in APPENDIX D, t can be obtained by

$$t = \begin{bmatrix} \cos t_1 \\ \sin t_1 \\ \cos t_2 \\ \sin t_2 \end{bmatrix} = \begin{bmatrix} \mu_1 \\ \mu_2 \\ m_1\mu_1 + n_1\mu_2 + q_1 \\ m_2\mu_1 + n_2\mu_2 + q_2 \end{bmatrix}, \tag{89}$$

where

$$\begin{cases} u = \begin{bmatrix} \mu_1 & \mu_2 & \mu_3 & \mu_4 \end{bmatrix}^T, \\ m_1 = \dfrac{a_1}{a_2} \cos(\beta_1 - \beta_2), n_1 = -\dfrac{b_1}{a_2} \sin(\beta_1 - \beta_2), \\ q_1 = \dfrac{1}{a_2} [(x_1 - x_2) \cos\beta_2 + (y_1 - y_2) \sin\beta_2], \\ m_2 = \dfrac{a_1}{b_2} \sin(\beta_1 - \beta_2), n_1 = \dfrac{b_1}{b_2} \cos(\beta_1 - \beta_2), \\ q_1 = \dfrac{1}{b_2} [(x_2 - x_1) \sin\beta_2 + (y_1 - y_2) \cos\beta_2]. \end{cases} \tag{90}$$

According to trigonometric function relation, we have the following restrictions:

$$\begin{cases} {\mu_1}^2 + {\mu_2}^2 = 1, \\ (m_1\mu_1 + n_1\mu_2 + q_1)^2 + (m_2\mu_1 + n_2\mu_2 + q_2)^2 = 1. \end{cases} \tag{91}$$

Substituting (89) into (83), the coordinates of the target can be obtained by

$$\begin{cases} x_{tar} = a_1 \cos\beta_1\mu_1 - b_1 \sin\beta_1\mu_2 + x_1, \\ y_{tar} = a_1 \sin\beta_1\mu_1 + b_1 \cos\beta_1\mu_2 + y_1. \end{cases} \tag{92}$$

REFERENCES

[1] J. L. Krolik, J. Farrell, and A. Steinhardt, "Exploiting multipath propagation for GMTI in urban environments," in *Proc. IEEE Conf. Radar*, Verona, NY, USA, Jun. 2006, pp. 1–4.

[2] B. Chakraborty, Y. Li, and J. J. Zhang, "Multipath exploitation with adaptive waveform design for tracking in urban terrain," in *Proc. IEEE Int. Conf. Acoust., Speech Signal Process.*, Dallas, TX, USA, Mar. 2010, pp. 3894–3897.

[3] R. Linnehan and J. Schindler, "Multistatic scattering from moving targets in multipath environments," in *Proc. IEEE Radar Conf.*, Pasadena, CA, USA, May 2009, pp. 1–6.

[4] F. Ahmad, M. G. Amin, and S. A. Kassam, "Synthetic aperture beamformer for imaging through a dielectric wall," *IEEE Trans. Aerosp. Electron. Syst.*, vol. 41, no. 1, pp. 271–283, Jan. 2005.

[5] Y.-S. Yoon and M. G. Amin, "Spatial filtering for wall-clutter mitigation in through-the-wall radar imaging," *IEEE Trans. Geosci. Remote Sens.*, vol. 47, no. 9, pp. 3192–3208, Sep. 2009.

[6] F. Ahmad and M. G. Amin, "Through-the-wall human motion indication using sparsity-driven change detection," *IEEE Trans. Geosci. Remote Sens.*, vol. 51, no. 2, pp. 881–890, Feb. 2013.

[7] S. Guo, G. Cui, L. Kong, and X. Yang, "An imaging dictionary based multipath suppression algorithm for through-wall radar imaging," *IEEE Trans. Aerosp. Electron. Syst.*, vol. 54, no. 1, pp. 269–283, Feb. 2018.

[8] M. Wang, G. Cui, L. Kong, and X. Yang, "First-order rear-wall multipath positioning and suppression for through-wall imaging radar," *IEEE Sensors J.*, vol. 18, no. 20, pp. 8261–8274, Oct. 2018.

[9] H. Li, G. Cui, L. Kong, G. Chen, M. Wang, and S. Guo, "Robust human targets tracking for MIMO through-wall radar via multi-algorithm fusion," *IEEE J. Sel. Topics Appl. Earth Observ. Remote Sens.*, vol. 12, no. 4, pp. 1154–1164, Apr. 2019.

[10] A. Sume, M. Gustafsson, and A. Janis, "Radar detection of moving objects around corners," *Proc. SPIE*, vol. 7308, Apr. 2009, Art. no. 73080V.

[11] A. Sume, M. Gustafsson, M. Herberthson, A. Janis, S. Nilsson, J. Rahm, and A. Orbom, "Radar detection of moving targets behind corners," *IEEE Trans. Geosci. Remote Sens.*, vol. 49, no. 6, pp. 2259–2267, Jun. 2011.

[12] M. Gustafsson, A. Andersson, T. Johansson, S. Nilsson, A. Sume, and A. Orbom, "Extraction of human micro-Doppler signature in an urban environment using a 'sensing-behind-the-corner' radar," *IEEE Geosci. Remote Sens. Lett.*, vol. 13, no. 2, pp. 187–191, Feb. 2016.

[13] M. Gustafsson, A. Andersson, and T. Johansson, "Micro-Doppler extraction of a small UAV in a non-line-of-sight urban scenario," *Proc. SPIE*, vol. 10188, May 2017, Art. no. 101880U.

[14] R. Zetik, M. Roding, and R. Thoma, "UWB localization of moving targets in shadowed regions," in *Proc. 6th Eur. Conf. Antennas Propag. (EUCAP)*, Prague, Czech Republic, Jun. 2012, pp. 1729–1732.

[15] R. Zetik, M. Eschrich, S. Jovanoska, and R. S. Thoma, "Looking behind a corner using multipath-exploiting UWB radar," *IEEE Trans. Aerosp. Electron. Syst.*, vol. 51, no. 3, pp. 1916–1926, Jul. 2015.

[16] I. Rodriguez, H. C. Nguyen, and T. B. Sorensen, "Analysis of 38 GHz mmWave propagation characteristics of urban scenarios," in *Proc. 21th Eur. Wireless Conf.*, Budapest, Hungary, 2015, pp. 1–8.

[17] K. Thai, O. Rabaste, and J. Bosse, "Around-the-corner radar: Detection and localization of a target in non-line of sight," in *Proc. IEEE Radar Conf. (RadarConf)*, Seattle, WA, USA, May 2017, pp. 0842–0847.

[18] Q. Zhao, G. Cui, and S. Guo, "Millimeter wave radar detection of moving targets behind a corner," in *Proc. 21st Int. Conf. Inf. Fusion (FUSION)*, Cambridge, U.K., 2018, pp. 2042–2046.

[19] S. K. Doddalla and G. C. Trichopoulos, "Non-line of sight terahertz imaging from a single viewpoint," in *IEEE MTT-S Int. Microw. Symp. Dig.*, Philadelphia, PA, USA, Jun. 2018, pp. 1527–1529.
[20] A. Kirmani, T. Hutchison, J. Davis, and R. Raskar, "Looking around the corner using ultrafast transient imaging," *Int. J. Comput. Vis.*, vol. 95, no. 1, pp. 13–28, Oct. 2011.
[21] M. La Manna, F. Kine, E. Breitbach, J. Jackson, T. Sultan, and A. Velten, "Error backprojection algorithms for non-line-of-sight imaging," *IEEE Trans. Pattern Anal. Mach. Intell.*, vol. 41, no. 7, pp. 1615–1626, Jul. 2019.
[22] A. Velten, T. Willwacher, and O. Gupta, "Recovering three-dimensional shape around a corner using ultrafast time-of-flight imaging," *Nature Commun.*, vol. 3, no. 745, Mar. 2012.
[23] M. Buttafava, J. Zeman, A. Tosi, K. Eliceiri, and A. Velten, "Non-line-of-sight imaging using a time-gated single photon avalanche diode," *Opt. Express*, vol. 23, no. 16, p. 20997, Aug. 2015.
[24] S. Chan, R. E. Warburton, G. Gariepy, J. Leach, and D. Faccio, "Non-line-of-sight tracking of people at long range," *Opt. Express*, vol. 25, no. 9, p. 10109, May 2017.
[25] S. Fan, G. Cui, S. Guo, L. Kong, X. Yang, and X. Yuan, "Corner target positioning with unknown walls' positions," *J. Eng.*, vol. 2019, no. 19, pp. 6143–6146, Oct. 2019.
[26] S. Fan, Y. Wang, and G. Cui, "Moving target localization behind L-shaped corner with a UWB radar," in *Proc. IEEE Radar Conf.*, Boston, MA, USA, Apr. 2019, pp. 1–5.
[27] P. Setlur, M. Amin, and F. Ahmad, "Multipath model and exploitation in through-the-wall and urban radar sensing," *IEEE Trans. Geosci. Remote Sens.*, vol. 49, no. 10, pp. 4021–4034, Oct. 2011.
[28] G. Cui, L. Kong, and X. Yang, "Reconstruction filter design for stepped-frequency continuous wave," *IEEE Trans. Signal Process.*, vol. 60, no. 8, pp. 4421–4426, Aug. 2012.
[29] R. E. Kalman, "A new approach to linear filtering and prediction problems," *J. Basic Eng.*, vol. 82, no. 1, pp. 35–45, Mar. 1960.
[30] Y. Zhang, M. Amin, F. Ahmad, and S. A. Kassam, "Application of time-frequency analysis and Kalman filter to range estimation of targets in enclosed structures," in *Proc. IEEE Radar Conf.*, Rome, Italy, May 2008, pp. 1–4.

XIAQING YANG (Student Member, IEEE) received the B.S. degree in electronic engineering from the University of Electronic Science and Technology of China (UESTC), Chengdu, China, in 2013, where she is currently pursuing the Ph.D. degree in signal and information processing.

SHIHAO FAN received the B.S. degree from the Hefei University of Technology, Hefei, China, in 2017. He is currently pursuing the M.S. degree with the School of Information and Communication Engineering, University of Electronic Science and Technology of China (UESTC), Chengdu, China.

His research interest includes NLOS target detection in urban environment.

SHISHENG GUO (Member, IEEE) received the B.S. degree in communication engineering from Nanchang Hangkong University, Nanchang, China, in 2013, and the Ph.D. degree in signal and information processing from the University of Electronic Science and Technology of China (UESTC), Chengdu, China, in 2019.

He is currently an Associate Researcher with the School of Information and Communication Engineering, UESTC. His research interests include through-the-wall radar imaging, signal analysis, and NLOS target detection.

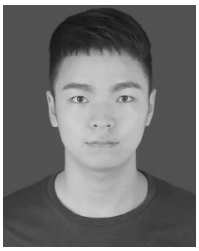

SONGLIN LI received the B.S. degree from the Chengdu University of Technology, Chengdu, China, in 2018. He is currently pursuing the M.S. degree with the School of Information and Communication Engineering, University of Electronic Science and Technology of China (UESTC), Chengdu.

His research interest includes NLOS target detection in urban environment.

GUOLONG CUI (Senior Member, IEEE) received the B.S. degree in electronic information engineering and the M.S. and Ph.D. degrees in signal and information processing from the University of Electronic Science and Technology of China (UESTC), Chengdu, China, in 2005, 2008, and 2012, respectively.

From January 2011 to April 2011, he was a Visiting Researcher with the University of Naples Federico II, Naples, Italy. From June 2012 to August 2013, he was a Postdoctoral Researcher with the Department of Electrical and Computer Engineering, Stevens Institute of Technology, Hoboken, NJ, USA. From September 2013 to July 2018, he was an Associate Professor with UESTC, where he has been a Professor, since August 2018. His current research interests include cognitive radar, array signal processing, MIMO radar, and through-the-wall radar.

WEI ZHANG received the B.S. degree in electronic engineering and the M.S. degree in circuits and systems from the University of Electronic Science and Technology of China (UESTC), Chengdu, China, in 2008 and 2011, respectively, where he is currently pursuing the Ph.D. degree in information and communication engineering with the School of Information and Communication Engineering.

From July 2011 to September 2018, he was an Engineer with the Science and Technology on Electronic Information Control Laboratory, where he has been a Senior Engineer, since January 2019. His research interests include electromagnetic big data analysis and signal information intelligent processing.